Percolating Reaction-Diffusion Waves (PERWAVES) — Sounding Rocket Combustion Experiments

Acta Astronautica 177 (2020) 639–651

Contents lists available at ScienceDirect

Acta Astronautica

journal homepage: www.elsevier.com/locate/actaastro

Research paper

Percolating Reaction–Diffusion Waves (PERWAVES)—Sounding rocket combustion experiments

Jan Palečka [a], Samuel Goroshin [a], Andrew J. Higgins [a], Yuriy Shoshin [b], Philip de Goey [b], Jean-Régis Angilella [c], Hergen Oltmann [d], Andreas Stein [d], Burkhard Schmitz [d], Antonio Verga [e], Sébastien Vincent-Bonnieu [e], Wim Sillekens [e], Jeffrey M. Bergthorson [a,*]

[a] Department of Mechanical Engineering, McGill University, 817 Sherbrooke Street West, Montréal, Québec H3A 0C3, Canada
[b] Department of Mechanical Engineering, Eindhoven University of Technology, P.O. Box 513, 5600MB Eindhoven, The Netherlands
[c] Normandie Université, UNICAEN, UNIROUEN, ABTE, ESIX Cherbourg, Caen 14000, France
[d] Airbus Defence and Space GmbH, Airbus-Allee 1, 28199 Bremen, Germany
[e] European Space Agency – ESTEC, Keplerlaan 1, 2201 AZ Noordwijk, The Netherlands

ARTICLE INFO

Keywords:
Microgravity science
Sounding rocket
Metal combustion
Percolation
Reaction–diffusion waves
Discrete combustion

ABSTRACT

Percolating reaction–diffusion waves in disordered random media are encountered in many branches of modern science, ranging from physics and biology to material science and combustion. Most disordered reaction–diffusion systems, however, have complex morphologies and reaction kinetics that complicate the study of the dynamics. Flames in suspensions of heterogeneously reacting metal-fuel particles is a rare example of a reaction–diffusion wave with a simple structure formed by point-like heat sources having well-defined ignition temperature thresholds and combustion times. Particle sedimentation and natural convection can be suppressed in the free-fall conditions of sounding rocket experiments, enabling the properties of percolating flames in suspensions to be observed, studied, and compared with emerging theoretical models. The current paper describes the design of the European Space Agency PERWAVES microgravity combustion apparatus, built by the Airbus Defense and Space team from Bremen in collaboration with the scientific research teams from McGill University and the Technical University of Eindhoven, and discusses the results of two sounding-rocket flight experiments. The apparatus allows multiple flame experiments in quartz glass tubes filled with uniform suspensions of 25-micron iron particles in oxygen/xenon gas mixtures. The experiments performed during the MAXUS-9 (April 2017) and TEXUS-56 (November 2019) sounding rocket flights have confirmed flame propagation in the discrete mode, which is a pre-requisite for percolating-flame behavior, and have allowed observation of the flame structure in the vicinity of the propagation threshold.

1. Introduction

1.1. Reaction-diffusion waves in random media

Waves propagating in reaction–diffusion systems are phenomena encountered at scales as varied as cellular biology to astrophysics [1]. Starting with the pioneering studies of Turing [2], waves in reaction–diffusion systems have been found to account for much of the pattern formation in nature. In the 1980s, the potential for a reaction–diffusion equation with a white-noise term, the Kardar–Parisi–Zhang (KPZ) equation [3], to describe quantitatively the dynamics of front propagation in a wide class of problems (e.g., turbulent liquid crystals, crystal growth, etc.) was discovered. By the 1990s, computer simulations of flames in two-dimensional random media [4,5] and experiments with smoldering fronts propagating in the disordered media of a sheet of paper [6] were also found to belong to this universality class; the inherent random nature of discrete media acts as the stochastic forcing found in the KPZ equation. These results suggested that combustion waves (i.e., flames) in random media may fall into this universality class.

1.2. Flames in suspensions of solid particulates: The discrete regime

Flames in many applications involving condensed-phase combustible matter can be represented as reaction–diffusion waves with distributed discrete sources. Forest fires propagating from tree to tree, combustion of pulverized solid fuel, self-propagating high-temperature synthesis (SHS), and energetic materials used as solid

* Corresponding author.
E-mail address: jeff.bergthorson@mcgill.ca (J.M. Bergthorson).

https://doi.org/10.1016/j.actaastro.2020.07.033
Received 15 May 2020; Received in revised form 13 July 2020; Accepted 21 July 2020
Available online 25 July 2020

propellants are all systems with randomly positioned sources of heat that are spatially localized. The question of the effect of randomness was also studied in particulate clouds. Comparisons of the characteristic flame length (combustion zone and preheat zone) with the distance between particles led to the conclusion that spatial discretization of sources was not required and the effect of heat sources could be approximated by a uniform release of heat, not that different from how gaseous flames are modeled. However, these considerations were often based on models which implicitly assumed continuous flame fronts to begin with [7].

Over the last two decades, researchers [8–12] have developed an analytic model of flames in systems with spatially localized sources. These models are an idealization of a reactive suspension of non-volatile fuel particles in an oxidizing gas. Since the system is characterized by large interparticle distances that exceed the particle size by two orders of magnitude, the reactive particles can be considered as point-like heat sources in space. The fuel particle starts to react when the value of the scalar field, i.e., temperature, reaches the ignition temperature of a single particle. After ignition, the particle combustion proceeds to completion with a rate that is practically independent of the transient temperature of the surrounding gas. The key element of the model for this system is the identification of a discreteness parameter $\chi = t_c\alpha/l^2$, which is the ratio of the particle combustion time, t_c, to the characteristic time of heat transfer in the space between neighboring particles, $t_h = l^2/\alpha$ (here l [cm] is interparticle distance and α [cm^2/s] is the thermal diffusivity). Interestingly, this model and the identification of the discreteness parameter also share the same mathematical formulation as models of Ca^{2+} waves in inter- and intracellular communication [13]. Studies with these analytical models have found that with small values of the parameter χ, the flame propagates in the *discrete regime* with a speed that is practically independent of the particle combustion time. Flames in the discrete regime also manifest other unusual properties:

- For a system with particles regularly distributed in space, for example, in the form of a cubic grid, the flame cannot propagate below a certain fuel concentration even if it generates flame temperatures that are nearly twice the ignition temperature of a single particle [10].
- When the particles are randomly positioned, fluctuations of their local concentration allow the flame to propagate closer to — or even exceeding — the thermodynamic limit [12].
- The flame in discrete systems exhibits front-roughening dynamics (illustrated in Fig. 1) that are described by the same power law exponent of $\beta = 1/3$ found in the KPZ universality class [14].
- For discrete flames in channels or cylinders with heat losses to the surroundings, the flames exhibit anomalous dimensional scaling in comparison to the classical value found for continuum flames [15].

For large values of the parameter χ, the dynamics of the front revert back to the continuum behavior of classical flames, in accordance with the correspondence principle required by fundamental models.

1.3. Experimental observation of discrete percolating flames and the need for microgravity experiments

Laboratory experiments conducted in the last decade have provided preliminary evidence for a key prediction of discrete flame theory: the independence of flame speed on oxygen concentration of metal fuels (e.g., aluminum, iron) under fuel-lean conditions [16–18]. Ground-based experiments are complicated by two significant problems. First, the difficulty in suspending sufficiently large particles: large particle sizes are necessary to avoid acoustic instabilities associated with small burning particles (i.e., acoustic coupling), and large particles enable the structure of the flame to be observed at the scale of individual particles. Settling of particles at high concentration can form turbulent

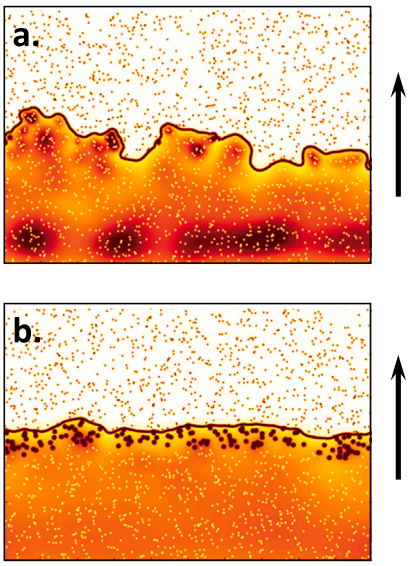

Fig. 1. Effect of discreteness parameter on flame front: Thermal structure of a flame front in a particle suspension as a function of the discreteness parameter, χ, for (a) small value ($\chi = 0.4$) and (b) a large value ($\chi = 3.2$) of the parameter. Arrows indicate the direction of flame propagation.
Source: Reprinted from [11].

recirculation cells that would inhibit laminar flame propagation [19]. Second is the fact that the low flame speeds encountered in the limit of a small discreteness parameter (order of 1 cm/s) makes the flames susceptible to disruption by buoyancy. Ground-based experiments are limited to micron-scale particulates and flame speeds typically exceeding 20 cm/s to avoid flame quenching due to buoyancy. Experiments aboard parabolic flight aircraft, with gravity levels at 2–5 $\times 10^{-2}g$, have been used to study flame propagation in suspensions in the discrete regime [11]. As shown in this paper (see Part 4), these levels are still sufficient for the residual acceleration to strongly affect both flame speed and its structure. Due to the dependence of buoyancy-driven flow on gravity, the minimal observable flame speed is proportional to $g^{1/3}$ [20]. Thus, to reduce the flame speed from that observable on parabolic flight aircraft by a factor of ten necessitates conducting sufficiently long-duration experiments in very low residual accelerations ($10^{-5}g$), which can only be afforded by sub-orbital or orbital microgravity platforms.

Microgravity has long been viewed as the ideal environment to overcome the particle sedimentation and buoyancy-driven disruption problems and, thus, studies that exploit freefall to study combustion in clouds of metal particulates date back four decades [21]. The recent Saffire experiments performed onboard the Cygnus vehicle studied flame propagation — free of buoyancy-driven flow — across a disordered material (cotton fabric) in microgravity. A roughened front was observed to propagate, but as this experiment was motivated by fire safety considerations, this particular aspect of the experiment was not further analyzed [22]. Microgravity has also recently been used to examine flame propagation in two-dimensional arrays of fuel droplets [23]. In these experiments, conducted on the Japanese Experiment Module (Kibo) on the International Space Station, n-decane droplets were randomly positioned on a square lattice of wires. Due to the local, droplet-to-droplet propagation mechanism, the resulting flames in these experiments can be interpreted using the concept of a percolation threshold. Percolation finds application in flames propagating in other types of disordered media, such as in propellants [24] and in SHS [7,25,26], in which flame propagation proceeds by direct contact between reactive sites. For a diffusion-controlled scalar field, such as fuel particulates in gas, the accumulated heat at the front

from previously ignited sources may make flames in these systems not amenable to classical percolation theory. The transition to percolation behavior by limitation of the long-range accumulation of heat sources via introduction of a loss term was recently explored [27,28].

Realization of a well-characterized, three-dimensional system that is random, without arbitrary positioning of sources, is the objective of the program presented in this paper, named Percolating Reactive Waves (PERWAVES). The name reflects the percolating-like appearance of the flame, which bears a striking visual resemblance to the spread of infectious disease through a population or the seeping of fluid through porous media, but the medium between sources is governed by a continuum scalar field (i.e., gas temperature) rather than the site or bond connectivity of classical percolation. This program utilizes the freefall conditions provided by sounding rockets, drawing upon experience obtained by McGill University in the 1990s and 2000s using parabolic flight aircraft to study flames in particulate suspensions [29]. Research teams at McGill University (Montreal, Canada) and Eindhoven Technical University (Eindhoven, the Netherlands) are responsible for the theoretical and ground-based part of the experimental research program, whereas development of the space hardware and the technical support of its flight operations is provided by the Airbus team (Bremen, Germany). The current paper presents the design of the PERWAVES space hardware and the results of the experiments performed aboard the MAXUS-9 and TEXUS-56 sounding rockets [30] launched in April 2017 and November 2019, respectively, from the Esrange Space Center (Sweden). It also describes parabolic flight experiments performed in summer 2019 with the TEXUS-56 apparatus that tested some new technical solutions in preparations for the sounding-rocket experiment.

1.4. Novel applications of metal combustion

Over the last century, interest in metal combustion was fueled by traditional applications of metals as fuels in solid-state rocket propellants [31,32], energetic materials [33], and by the demand to provide industrial safety in the numerous technological processes featuring metal powders [34,35]. Nowadays, there is a renewed interest in metal fuels as recyclable, carbon-free metal energy carriers [36–38] as well as prospects of using metal propellants for in-situ resource utilization (ISRU) in future missions [39,40]. While, in these applications, metal flames would operate in conditions different than the idealized environment of the PERWAVES experiment, a deeper understanding of the fundamental processes of metal particulate combustion will be obtained from microgravity-based studies. This understanding would enable a science-based development of these new energy carrier technologies, in comparison to the empirical-based development of combustion technologies in the 19th and 20th centuries.

Being free of carbon and having volumetric energy densities greater than hydrocarbons, metal fuels are able to burn and generate clean heat without carbon-dioxide emissions [38]. The solid-state metal oxide combustion products can be easily separated from the hot gas flow and then stored and shipped for recycling at metal smelters powered by clean energy sources [37]. The heat produced by metal flames can be efficiently converted to motive power, or can be used to generate electricity, using external-combustion heat engines or water boilers coupled to steam turbines. The metal-fuel cycle represents an easily scalable technology that permits storage and trade of green energy on a global scale [37].

Metals are also of interest as potential fuels in future space missions to the Moon, Mars, and beyond. The feasibility of affordable and sustainable interplanetary transportation relies, to a large extent, on the ability to manufacture propellants using local materials, i.e., for in-situ resource utilization (ISRU). Thus, instead of bringing fuel for the return trip all the way from the Earth, the metal fuel and oxygen for the propellant can be produced from the metal oxides in lunar or planetary soils using solar or nuclear energy. Several light metals such as aluminum and magnesium can also efficiently burn with carbon dioxide, which is the main component of the Martian atmosphere. Thus, metal fuels burning with CO_2 can be used not only for the return mission from Mars to Earth but also for on-planet Martian transportation [39,41].

2. Design and operational procedure of the MAXUS-9 PERWAVES experiment

2.1. PERWAVES hardware design principles

The working principle of the PERWAVES sounding-rocket module is based on the "flame in a semi-open tube" concept successfully used since the 1990s by McGill researchers for experiments with metal flames aboard parabolic flight aircraft [29]. As illustrated in Fig. 2, a laminar flame is initiated at the open end of a glass tube and propagates towards the closed end through a quiescent metal suspension at constant ambient pressure, allowing easy observation and spectral diagnostics of the flame. The overall design of the MAXUS-9 sounding rocket experimental module is shown in Fig. 3.

The oxidizing gas mixtures are stored in high-pressure reservoirs and are supplied to the test sections through pressure regulators. The gas, maintained at a steady flow of about 70 cm^3/s by a flowmeter, enters the dispersion system through a narrow rectangular (20 mm ×

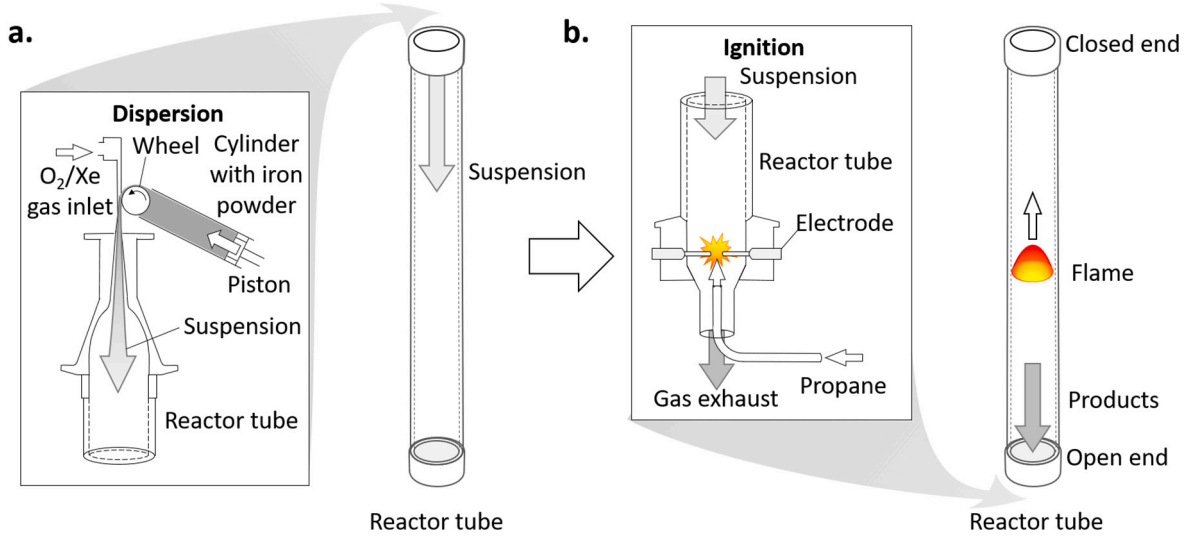

Fig. 2. Design principles: Description of the (a) particle dispersion and (b) ignition systems and their respective positions with respect to the reactor tube.

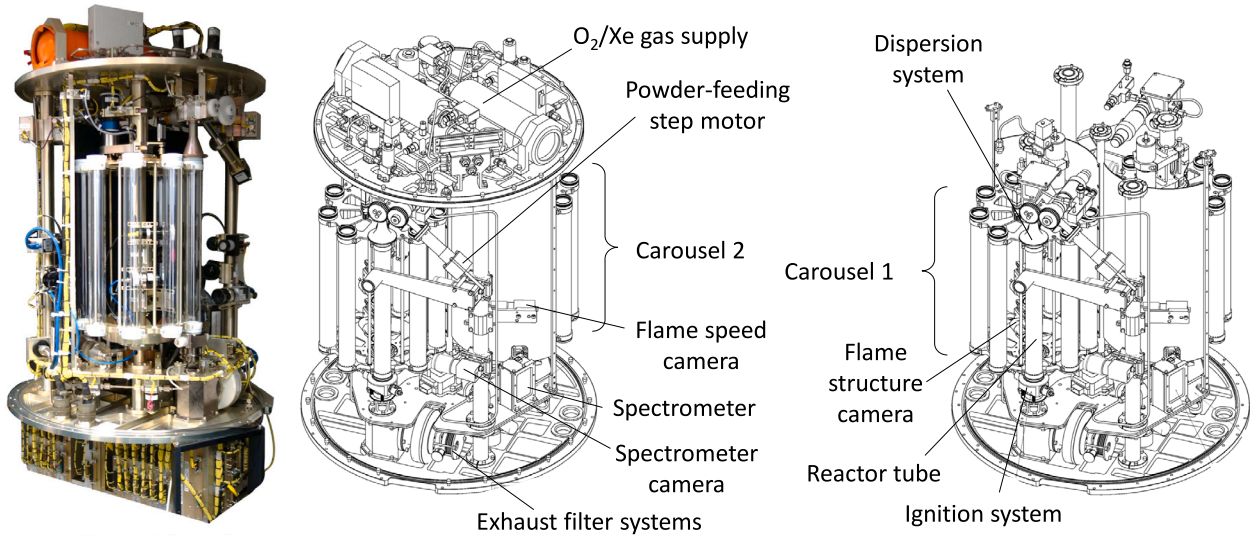

Fig. 3. Experimental apparatus: Photo of the apparatus and schematics illustrating its different parts.

1 mm) channel. The metal powder, stored in a cylindrical reservoir, is pushed towards the channel by a piston connected to a linear actuator driven by a variable-speed step motor (see Fig. 2(a) inset). The particles, fed onto and collected by a rotating wheel with a rough surface, are deposited into the gas flow in the narrow channel. A relative uniformity of the dispersed suspensions was confirmed by prior lab and drop-tower experiments. After expansion in a bell-shaped conical diffuser (Fig. 2(a)), the flow of suspended particles enters a quartz tube (inner diameter: 30 mm, length: 332 mm). After dispersing the volume equivalent of about two full tubes, the gas flow is stopped. Within a delay of 0.4 s, about 1 cm^3 of propane is injected into the tube at the open end and is ignited by an electrical spark (see Fig. 2(b)). The propane combustion, in turn, ignites the particles and a flame propagates through the quiescent suspension towards the closed end of the tube. Both the gas/particle mixture before ignition, and the combustion products leaving the tube after ignition, are picked up by the exhaust flow, driven by a fan, through a multilayered exhaust HEPA filter, which collects all micron- and submicron-sized solid particles.

2.2. Optical diagnostics

Each carousel in the PERWAVES apparatus is provided with three CMOS cameras (Fig. 4). A Basler ace acA2000-50gm camera, operated at 60 Hz with a resolution of 2048 × 280 pixels, has a field-of-view of 30 cm × 4 cm spanning the entire tube length and is used for flame speed measurements. A Basler ace acA1300-60gm with a 1024 × 1024 pixel resolution is focused on a 3 cm × 3 cm section in the middle of the tube, providing a close-up image of the flame for the study of its structure. Another Basler ace acA1300-60gm camera, with a resolution of 1280 × 824 pixels, operated at 10 Hz with a field-of-view of about 3 cm × 2 cm, is focused on particles illuminated by a thin rectangular 0.1 cm × 3 cm laser light sheet, which is used for estimations of the iron fuel concentration by recording, and later counting, illuminated particles. The green diode laser beam (wavelength of 520 nm) for particle illumination has a boosted power of about 70 mW before it enters the prism used for creating the light sheet of about 10 mW. An Ocean Optics USB-2000 fiber spectrometer with a spectral resolution of about 1.5 nm records flame spectra at a rate of about 20 spectra per second from a 2-mm-diameter spot in the middle of the glass tube. The spectra are used to determine the combustion temperature of the reacting particles by multi-wavelength pyrometry. A single Pokini I type computer controls all cameras and the spectrometer and enables, as well, a live conversion of the digital signal to analog output for the downlink to the ground control station.

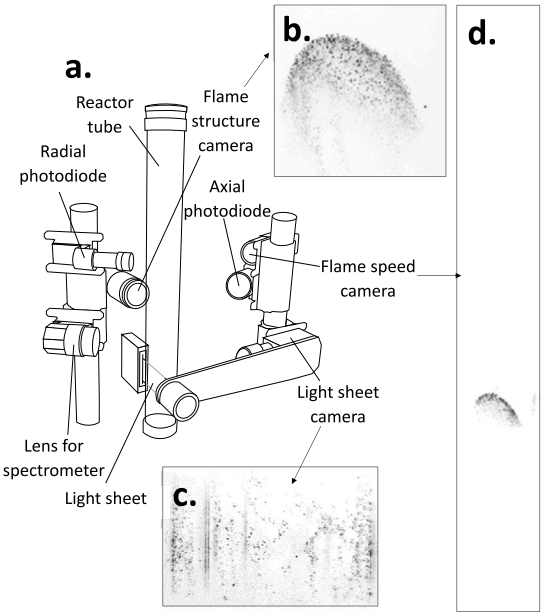

Fig. 4. Optical diagnostics: (a) Schematics of diagnostics of the PERWAVES apparatus, and images of (b) the close-up image of the flame, (c) the particles illuminated by the laser sheet, and (d) the overall view of flame propagation in the tube. Negative images are presented for clarity.

2.3. Operational procedure

The automated test procedure, described below, relies on signals from two photodiodes, which monitor the progress of the flame in the tube. An axial photodiode (see Fig. 4), is used to confirm the onset of the flame in the tube. The second radial diode detects and confirms the successful propagation of the flame past the middle of the tube (Fig. 4).

The operation of the PERWAVES apparatus, including the decision-making algorithm for changing the feeding rate of iron into the tube, was fully automated. The first experimental run was performed at a pre-determined particle feeding rate. Based on the readings of the photodiodes, the feeding rate for the next run was decreased or increased. A successful propagation event, indicated by the signal from the second photodiode, was followed by a run with an incremental decrease in the feeding rate of iron. An absence of ignition, or premature flame

extinction in the tube, indicated by the lack of signal from the first and second photodiodes, respectively, was followed by an incremental increase in the feeding rate. Reduced-resolution videos, transmitted live via a communication link to ground control, allowed operators to directly observe flame propagation. The up-link to the payload also permitted the operators to override the algorithm-guided procedure by manually decreasing/increasing the iron feeding rate as well as extending the 25-s interval initially allocated by the algorithm for flame observation.

2.4. Iron powder and gas mixtures

Iron was selected as the fuel since it primarily reacts in the condensed phase through heterogeneous surface oxidation. The experiments were performed with 99.8%-pure spherical iron powder manufactured by TLS Technik (Germany). The powder was sieved to a narrow particle size distribution shown in Fig. 5 in the range 20–30 μm. The use of xenon (a heavy noble gas) as the diluent gas in the oxidizer was done to lower the thermal diffusivity of the medium in which the particles are suspended, so that the reactive wave propagates in the discrete regime. Two oxygen/xenon gas mixtures with oxygen contents of 20% and 40% by volume were used as carrier gases in particle–gas suspensions. The combustion times of iron particles in these oxidizing mixtures were measured in laboratory experiments by high-speed filming of the combustion of a very diluted particle suspension injected into a quartz tube preheated to about 1100 K [42]. The average combustion time in the 20% O_2/80% Xe gas mixture was found to be about 8.1 ms whereas, in the 40%-oxygen mixture, it was less than 2.7 ms, i.e., about three times shorter. The estimated ignition temperature of iron particles in both mixtures was similar, within an accuracy of about 100 K, and was found to be around 1000 K.

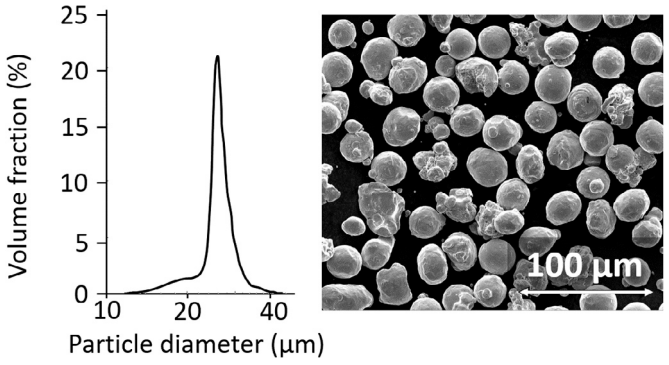

Fig. 5. Iron powder: (a) Size distribution of the iron particles obtained with the Beckman-Coulter 4e-Multisizer and (b) the scanning electron microscope photograph of the iron powder.

3. MAXUS-9 sounding rocket flight and experimental results

3.1. Experiment objectives

The main objective of the PERWAVES experiments performed on board the MAXUS-9 sounding rocket was to obtain direct experimental evidence of the discrete flame propagation regime that is a prerequisite for the existence of percolating flames. Estimations of the discreteness parameter, χ, based on the combustion times of iron particles measured in the laboratory and known values of molecular heat transfer parameters in oxygen/xenon mixtures, indicate values for χ of about 0.15 for the mixture with 20% O_2 and 0.063 for oxygen/xenon mixture with 40% O_2, i.e., well within the discrete flame regime ($\chi \ll 1$) [42]. The most obvious feature that distinguishes the discrete-flame propagation regime from traditional homogeneous and continuous flames is the theoretical prediction that the flame speed is independent of the particle combustion time. Thus, in spite of the more than three times difference in particle combustion times in mixtures with 20% and 40% oxygen content, the flame speed is predicted to be practically the same in the discrete flame propagation mode, whereas classical flame theory predicts a difference between the two flame speeds of 1.9 times [42].

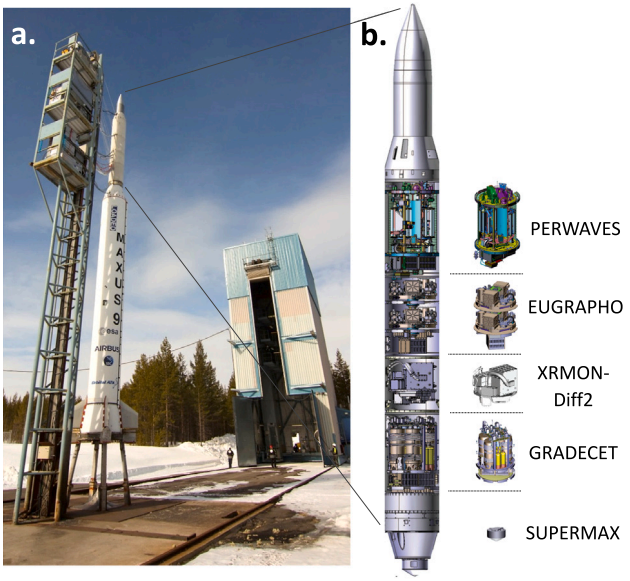

Fig. 6. MAXUS-9 sounding rocket: (a) the rocket on the launch site in front of the retractable enclosure, (b) diagram of the payload showing the experimental modules.

Fig. 7. MAXUS-9 flight: (a) Launch of the rocket from the Esrange site (credit: Neil Melville), (b) separation of the Castor IV rocket booster (long cylindrical section) and of the SUPERMAX parachute testing module (circular object in front), with a view of spring-loaded bolts (upper left and right). The picture is a still image from the Swedish Space Corporation (SSC) video taken by a camera placed on the bottom of the rocket payload (courtesy of SSC).

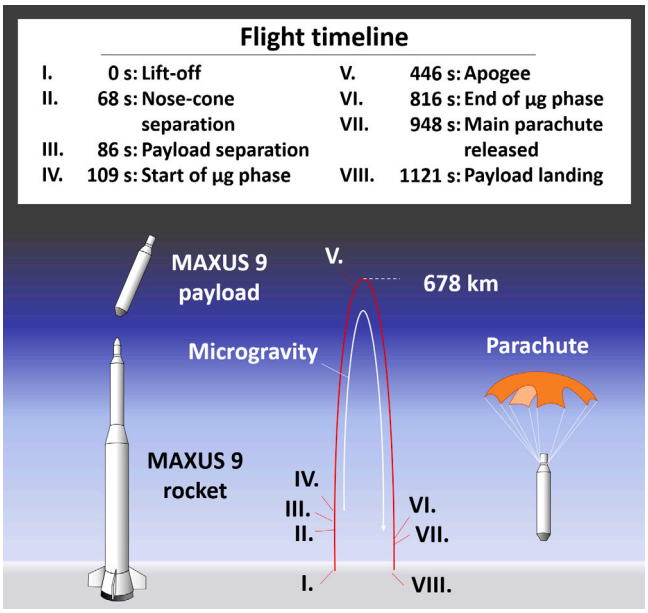

Fig. 8. Timeline of the MAXUS-9 flight stages.

3.2. MAXUS-9 sounding rocket flight parameters

In addition to PERWAVES, three other scientific experiments were flown on MAXUS-9: the EUGRAPHO experiment that studied the response of a single-cell algae to different gravity levels, XRMON-Diff2 that consisted of chemical diffusion experiments for semiconductor as well as for metallic material couples with in-situ X-ray monitoring, and GRADECET [43] that investigated gravity-dependent changes in the solidification process of metal alloys. The payload also included SUPERMAX, a drop capsule that was released for testing right after the separation of the rocket motor from the payload in order to test a supersonic parachute. Along with the nosecone section, the payload module (Fig. 6(b)) measured about 6.5 m in length and had a total mass of about 849 kg.

The payload was mounted on a single-stage Castor IVB solid-fuel rocket motor manufactured by Orbital ATK, USA. The MAXUS-9 sounding rocket was launched from the Esrange Space Center in Sweden on April 7th, 2017, at 11:30 CEST (Fig. 7(a)). After separation from the booster, the residual rotation of the payload section was stopped by tangential gas jets, and the payload followed a ballistic trajectory reaching an apogee of about 678 km (Fig. 8). All scientific experiments on board were initiated at 109 s after lift-off when the gravitational acceleration fell below the threshold value of $10^{-4}\,g$. Microgravity conditions in the 10^{-4} to $10^{-5}\,g$-range were maintained for about 707 s. During re-entry, once the accelerometers exceeded the threshold value of $10^{-4}\,g$, the experiments were stopped, and the payload spin was started. During ballistic re-entry, the deceleration level of the payload reached 38.9 g. The parachute-assisted touchdown occurred at 1120 s (18 min 40 s) at about 79 km from the launch site. The experimental modules were recovered and returned to the launch site by a helicopter five hours after landing.

In total, 41 combustion runs (21 in the 20%-O_2 mixture and 20 in the 40%-O_2 mixture) were performed by the PERWAVES module during microgravity time. There was a considerable intervention in the experiment procedure by the ground crew that frequently overrode the automatic experiment algorithm. The intervention was dictated by a smaller than expected flame speed that required a prolongation of the time allocated for flame propagation by the algorithm in some runs. Sometimes, the flame propagation time was cut short when the flame was deemed steady enough for measuring flame speed. In other cases, operators overrode algorithm decisions to increase or decrease powder feeding rate in order to observe flame propagation at the same fuel concentration as the preceding run.

3.3. Measurement of the particle concentration in suspension

The concentration of iron particles in suspension was determined by a direct count of particles from a central section of volume illuminated by the laser sheet (Figs. 4 and 9). Average particle counts were obtained from about 40 CMOS camera frames when the particle count reached a steady-state value. The particle count, however, was found to be a relatively strong function of the camera sensitivity threshold. This is mainly due to a Gaussian intensity profile of the laser sheet exacerbated by far-field Fraunhofer diffraction from the light sheet-forming slit. The intensity profile of the laser sheet, which has no well-defined borders, makes the counting volume a function of the camera sensitivity, i.e., increasing the camera sensitivity leads to an increase of the volume from which particles are counted. This problem was resolved by a post-flight ground calibration of the particle counting system with suspensions of known concentrations of iron powder. The concentration of particles in the suspension was determined in ground-based experiments by measuring the mass feeding rate of the powder and of the gas mixture. The concentration was corrected to account for particle velocity slip with respect to the gas at normal gravity conditions. Using on-the-ground calibration, the in-flight iron fuel concentrations were found to be in the range between 0.5 and 1.1 g/L [42]. This value is close to the range of about 0.7–1.1 g/L estimated from the particle count at the mid-range camera sensitivity and by using 0.4 mm width of the counting volume equal to the Full-Width at Half-Maximum (FWHM) Gaussian laser sheet intensity profile. Combustion products were deposited on

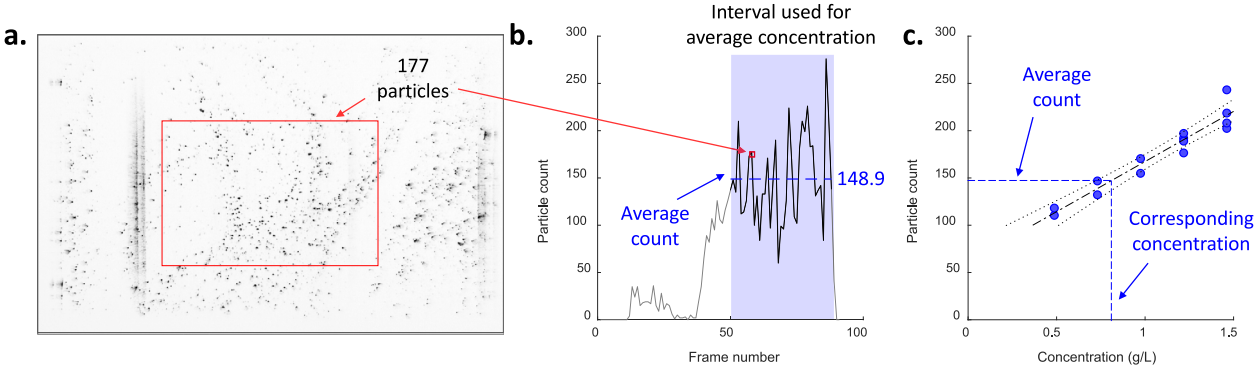

Fig. 9. Illustration of the post-flight data processing for measuring fuel mass concentration in suspension: (a) raw image binarization and subregion selection, (b) particle count from individual frames and the average count, (c) concentration determined through calibration curve obtained from ground-based tests (blue markers). (For interpretation of the references to colour in this figure legend, the reader is referred to the web version of this article.)

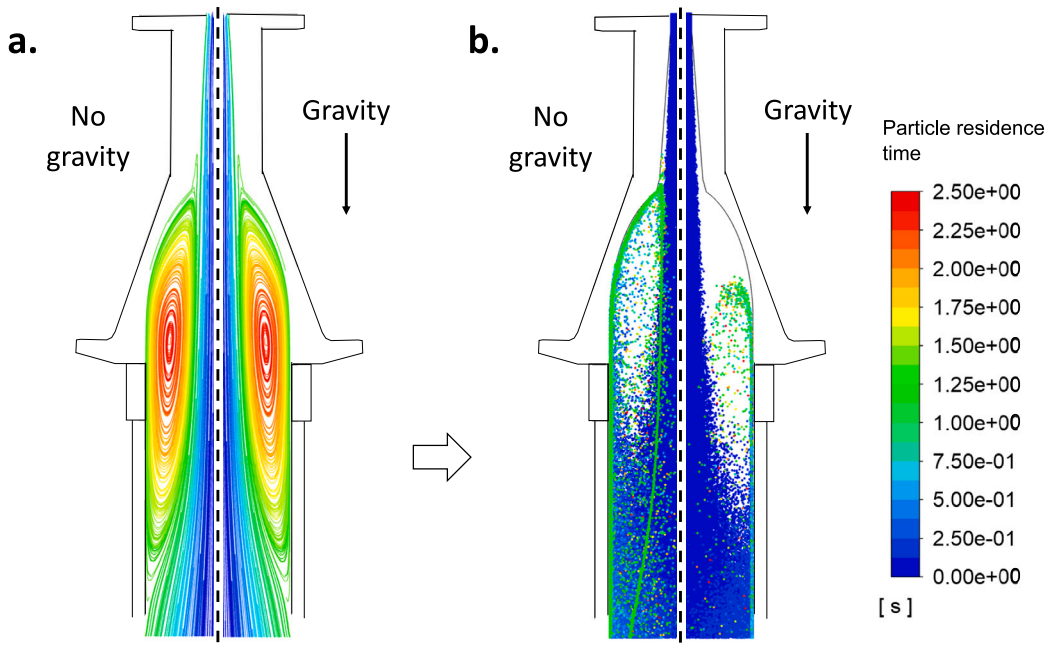

Fig. 10. Unsteady RANS (Reynolds-Averaged Navier–Stokes) simulations of the particle flow in the expansion cone and the combustion tube: (a) streamlines of gas flow and (b) dispersion of particles, colored by their residence time in the tube, under normal gravity and in microgravity. The particles start with zero velocity at the exit of the feeding channel. Images used courtesy of ANSYS, Inc.

the tube wall after the first combustion run (two combustion runs were performed in each tube), which attenuated the laser beam and reduced the particle image intensity and prevented accurate particle counts. Thus, for the second combustion run in the same tube, the concentration was estimated by extrapolating concentration data from runs in the clear tubes.

3.4. Peculiarities of particle dispersion in microgravity

On the ground, the particle counts in the flow obtained with the laser-sheet system were in good agreement with theoretical values calculated from the known powder feeding rates, the particle Stokes sedimentation velocity, and the volumetric gas flow rate. In microgravity, however, particle counts were found to be well below similarly calculated nominal values. The discrepancy suggests that, unlike at normal gravity conditions, in microgravity, not all powder supplied by the feeder goes into suspension and reaches the combustion tube. The results of flow simulations performed with ANSYS Fluent software [44], shown in Fig. 10, demonstrate a possible cause of this discrepancy. A sudden transition of the flow from the very narrow 2.0-mm slit into the expansion cone results in the formation of an axisymmetric vortex pair around the central flow stream (Fig. 10). For the mixtures used on MAXUS 9, the Stokes number, i.e., the ratio of the response time to the fluid convective time [45], was relatively low (≃0.04). Recent theoretical work [45,46] that investigated the motion of particles in two-phase flow in the vicinity of recirculation cells has shown that particles characterized by such low-Stokes numbers can be temporarily trapped by the vortex. This behavior can be observed in the absence of gravity (Fig. 10(b)). On the ground, however, gravity-induced sedimentation results in a much higher slip velocity between particles and the gas in the recirculating flow in the cell. Indeed, the calculated sedimentation speed (≃0.13 m/s) is comparable to the mean flow speed in the vicinity of the recirculation cell (≃0.2–0.3 m/s), so the gravity force is sufficient to pull the particles out of the vortex (Fig. 10(b)). The accumulation of particles on the walls of the expansion cone in low gravity was indeed confirmed experimentally during parabolic flight testing of the subsequent TEXUS-56 apparatus that employs a similar powder-dispersion unit. In some tests, the particles formed agglomerates which, after contact with the flame, detached and burned brightly in the tube over relatively long times. A more detailed theoretical analysis of the two-phase flow dynamics during the powder dispersion process in microgravity and on the ground will be performed in a dedicated publication.

3.5. Flame speed measurements

The flame speed was determined from the CMOS camera recordings using a filming rate of 60 frames per second. The field-of-view of the camera encompassed the entire length of the combustion tube. The position of the flame front on each frame was determined by taking the location of the farthest pixel that was illuminated above a specified threshold. The resulting curve was then smoothed by means of a simple algorithm and an example is shown in Fig. 11(a). The first 3 s of the flame propagation were discarded in order to avoid unsteady effects caused by the propane flame ignition. Only flame-propagation time intervals demonstrating a stable and steady flame over several seconds were used for the speed measurements. The flame speed for each experimental run was found as a mean of all interval speeds, weighted by the respective length of the time associated with each interval [42]. For every run, the uncertainty was taken as ±2 weighted standard deviations from the interval mean velocity.

A total of eight tests in each carousel exhibited regions with sufficiently linear traces for the determination of the steady state flame speed. In both mixtures, the flame propagated at the same speed, close to 1 cm/s, over the entire 0.5–1.0 g/L concentration range (Fig. 11(b)). In classical flame theory [47], the square of the flame speed is directly proportional to the fuel combustion rate, i.e., is inversely proportional to the particle combustion time. Thus, classical flame theory predicts that the flame speed should increase in the 40%-O_2 mixture by about 1.9 times in comparison to the 20%-O_2 mixture (see inset of Fig. 11(b)). On the contrary, discrete combustion theory [8] predicts that the flame speed is practically independent of the combustion time at very small values of the discreteness parameter. Discrete flame theory, therefore,

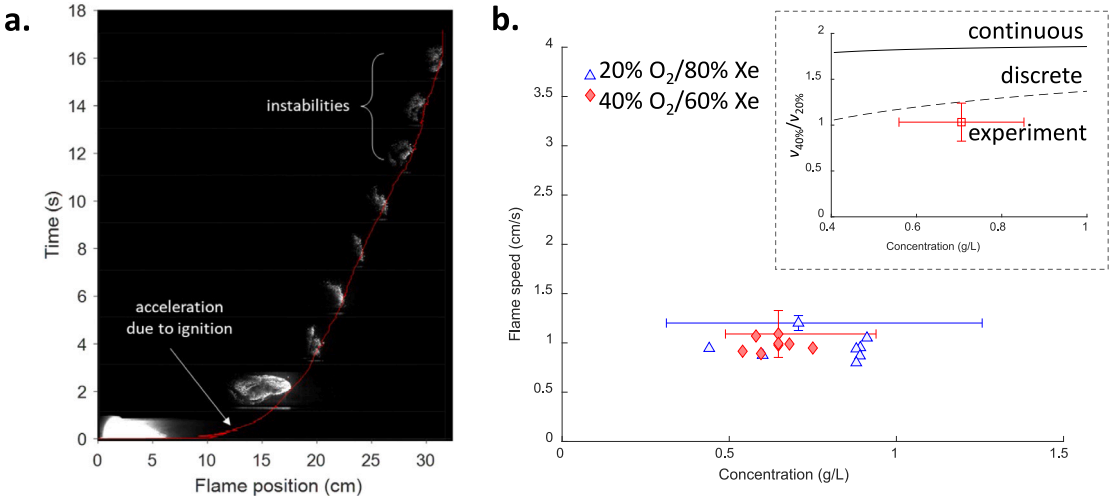

Fig. 11. Speed of the flame on MAXUS-9: (a) Flame trajectory (red curve) with images of the front taken at 2-second intervals, (b) Flame speed versus concentration in the 20%- and 40%-O_2 mixtures (from [42]). The inset of the figure shows that the ratio of experimental flame speeds is much closer to predictions of the discrete model.

predicts less than a 1.2 times increase in flame speed due to the small increase in the thermal diffusivity of the 40% O_2/60% Xe mixture in comparison to the 20% mixture. Thus, by measuring practically the same flame propagation velocities in 20%-O_2 and 40%-O_2 mixtures, the MAXUS-9 experiment provides direct evidence of the discrete flame propagation regime in iron–oxygen/xenon suspensions.

3.6. Flame temperature

The flame temperature of burning particles was determined by polychromatic fitting of the spectra acquired by the Ocean Optics USM-2000 spectrometer to Planck's law, based on the assumption that the flame continuous spectra are grey [29]. The flame temperatures in both 20%-O_2 and 40%-O_2 mixtures are found to be practically independent of the fuel concentration. In the 20%-O_2 mixtures, flame temperatures also demonstrated very little scatter (Fig. 12) and are close to the flame temperature predicted by the thermodynamic calculations performed with the FactSage software [48]. A significantly larger data scatter and departure from the thermodynamic prediction was obtained in the 40%-O_2 mixtures [42] and suggest that these spectra are not grey, i.e., flame emissivity is not independent of the light wavelength. Indeed, as shown in Fig. 12, a relatively strong system of the FeO molecular lines is evident on top of the continuous spectra. Scanning electron microscopy (SEM) and electron dispersive spectroscopy (EDS) of the combustion products also reveal that – unlike 20%-O_2 mixtures where oxide combustion products are mostly Fe_3O_4 black oxide, composed of particles larger than initial iron particles – the combustion products of the 40%-O_2 mixture contained a considerable amount of nano-size Fe_2O_3 red oxide [42]. Nanoparticles are known to demonstrate a strong dependence of the light emission and scattering on wavelength [49]. The presence of the FeO molecular lines and nano-size combustion products indicates at least partial vapor-phase combustion of iron particles in the 40% oxygen mixtures. This assumption correlates with particle images obtained in the ground-based experiments that show a distinct halo above the particle surface during the first stages of their combustion in the 40% oxygen [42]. The transition from the heterogeneous surface combustion observed at 20% O_2 content to combustion in the vapor phase at 40% O_2 results in shorter combustion times of iron particles than predicted by the simplified theory that assumes unchanged regime of the diffusion combustion [42,50].

4. TEXUS-56 sounding rocket PERWAVES experiment

Following the success of the PERWAVES experiment on MAXUS-9, further experiments were approved to study the structure and properties of flames in the discrete regime.

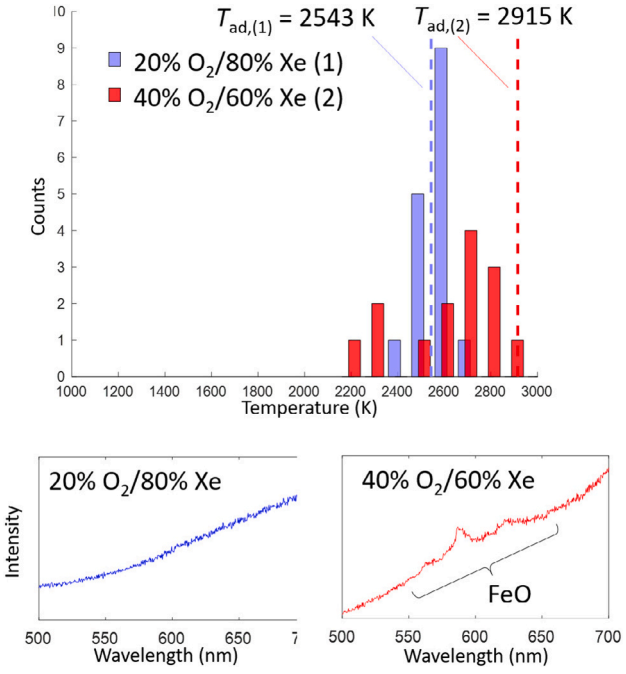

Fig. 12. Flame temperatures on MAXUS-9: Measured (histogram) and estimated (dash lines) iron flame temperatures (left) and spectra (right) in 20%-O_2 and 40%-O_2 oxygen/xenon mixtures. The adiabatic flame temperatures are estimated with the FactSage software [48].

4.1. TEXUS-56 PERWAVES apparatus modifications

In the next phase of the PERWAVES program, the experimental hardware developed for the large MAXUS payload was downsized to fit the smaller TEXUS-type rocket that has a more frequent flight schedule. The transition from the 0.64-m-diameter MAXUS payload to 0.44-m-diameter TEXUS hardware required the reduction of the experimental module to a single carousel with 9 tubes. Other design modifications, illustrated in Fig. 13, included the installation of an additional argon tank for a post combustion purging procedure that ensures quenching of any burning embers at the end of the combustion stage, replacement of the propane ignition system by a wire-ignition system, installation of a high-speed camera, and modification of the geometry of the expansion cone within the dispersion system.

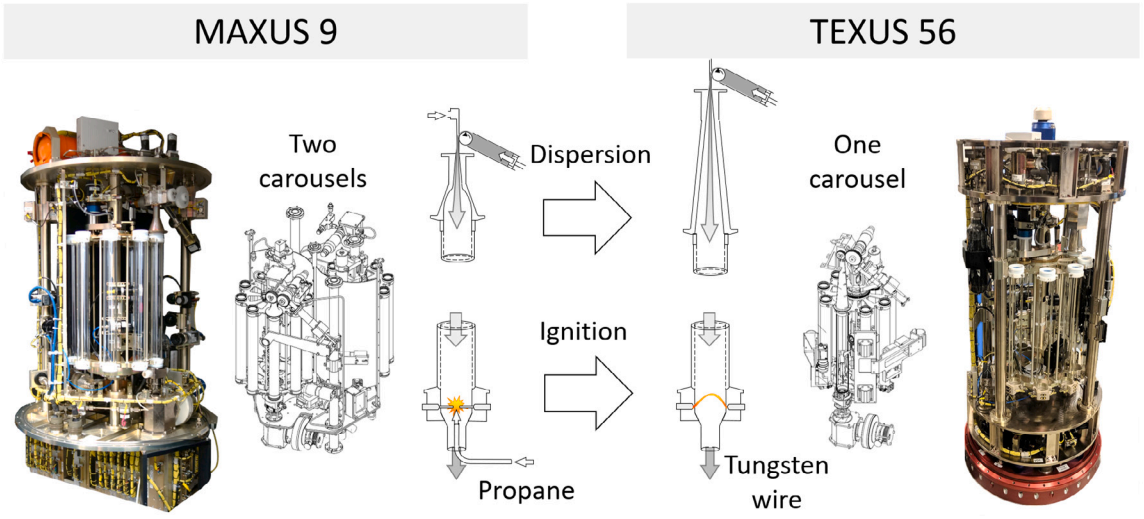

Fig. 13. Transition to TEXUS-56: Summary of technical modifications performed on the experimental module during the transition from Phase I to Phase II of the PERWAVES experiment.

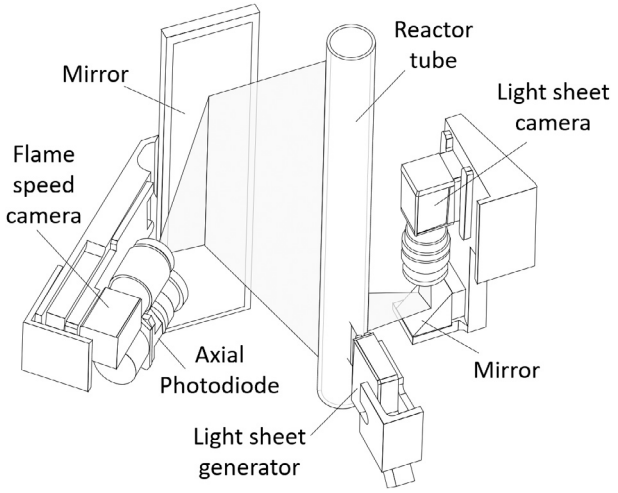

Fig. 14. TEXUS-56 diagnostics: Configuration of the diagnostics aboard the TEXUS experimental module, showing the main diagnostics, as well as the mirrors used to accommodate the lines-of-sight.

The propane-injection ignition system was replaced by an electrically heated tungsten-wire system similar to that previously used by McGill researchers in parabolic-flight combustion experiments [29]. The 0.125-mm-thick wire, fixed on a ring and stretched across the tube open end, was heated resistively by a 20-VDC electrical source, which initiated its self-sustained combustion at temperatures exceeding 3000 K [51]. Each reaction tube was equipped with two ignition wires. While the propane-ignition system resulted in sudden expansion of hot gas products, the wire ignition does not disturb the flame over long distances and, thus, permits reliable diagnostics of the flame parameters along the whole length of the combustion tube (see Fig. 20 below). A new 7° expansion cone connecting the dispersion channel with the combustion tube and increased flow rate to 140 cm^3/s were chosen in order to reduce particle trapping in microgravity (Fig. 13). A high-speed camera (Phantom Miro C210), with a field-of-view of 37.5 mm × 30 mm, at a resolution of 1280 × 1024 pixels (about 34.1 pixels/mm), permits the recording of flame propagation at about 1000 frames per seconds (fps). Real-time video uploading to the on-board permanent memory limited the length of each video to around

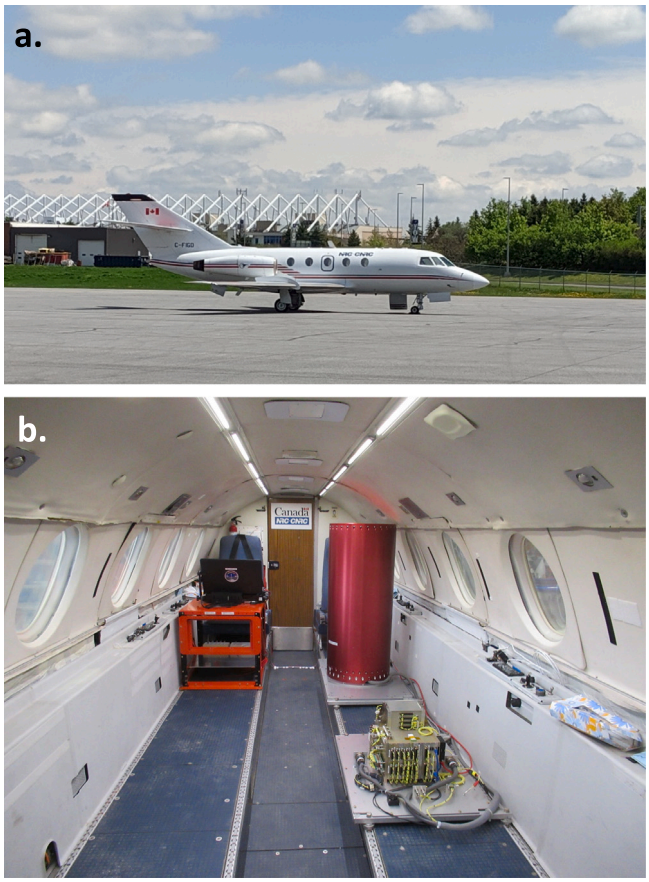

Fig. 15. Parabolic flights: (a) NRC Falcon-20 aircraft on runway, (b) Experimental apparatus, control unit, and laptop rack placed in the aircraft cabin.

2 s. The system of mirrors shown in Fig. 14 allows the line-of-sight of the video cameras to be maintained in a confined space.

4.2. Testing of the apparatus on parabolic flight aircraft

Prior to the TEXUS-56 sounding rocket flight, the performance of the modified apparatus was tested in the low-gravity environment

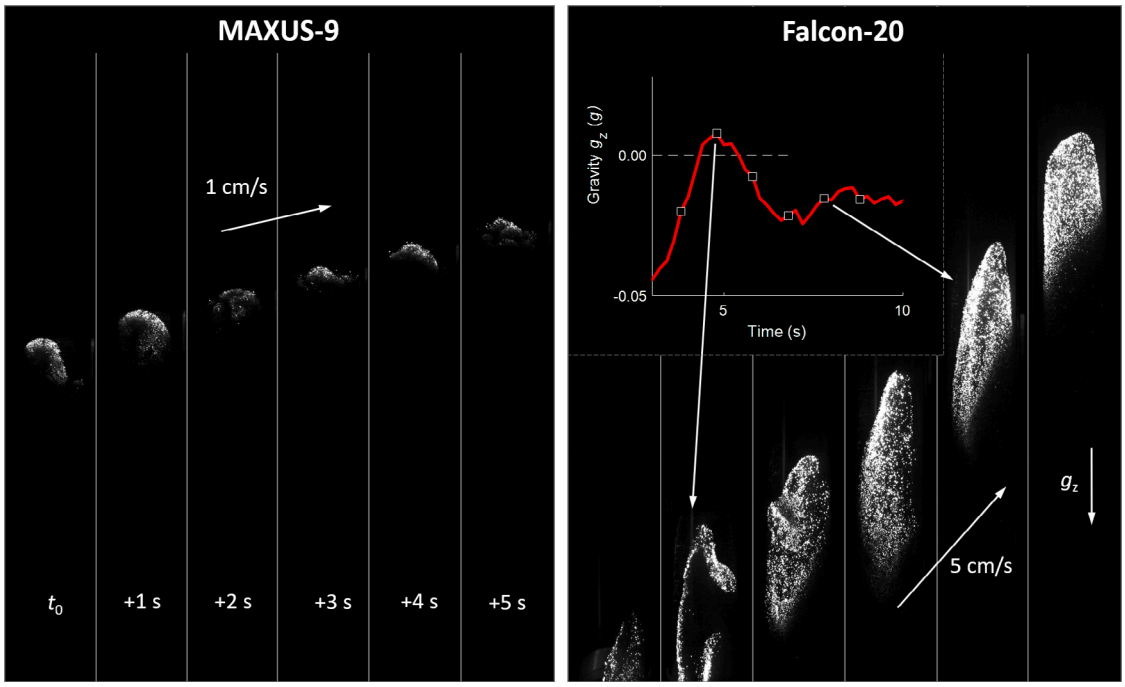

Fig. 16. Effect of level of microgravity on flame propagation: Comparison of the flame propagation on MAXUS-9 and Falcon-20 showing the difference in flame structure and speed due to the residual acceleration in the parabolic flights. The evolution of acceleration with time is shown for Falcon-20 at intervals of 1 s. For MAXUS-9, the effects are negligible in comparison.

provided by an aircraft flying along a parabolic trajectory. The microgravity platform, operated by the Canadian Space Agency (CSA) aboard the National Research Council of Canada (NRC) Falcon-20 aircraft, was used for the experiments. The campaign, conducted between May 27 and 31, 2019, included three flights with a total of 46 parabolas. Each parabola provided about 20 s of low-gravity time with typical levels of the acceleration, g_z, of about $10^{-2}g$ in the axial direction of the flame tube. The apparatus was tested in the same configuration as was later used in the sounding rocket flight and was enclosed within the sealed section of the rocket payload. The pictures of the Falcon-20 aircraft and the configuration of the payload on board the aircraft are shown in Fig. 15.

Parabolic flight testing confirmed that the wire-ignition system operated reliably, as did the modified optical diagnostic equipment. It is interesting to note that the flame propagation speeds measured in parabolic flights, with the same iron powders and oxidizing-gas mixture as the ones used in the previous MAXUS-9 sounding rocket experiments, were from 3 to 5 times greater, demonstrating the strong effect of residual gravity on the flame. As shown in Fig. 16, this increase in velocity is accompanied by a significant stretching of the flame front. While a satisfying explanation of this phenomenon requires more involved modeling efforts, some insight can be provided by estimations based on the analysis in [20]. As for most flames, the velocity induced by buoyancy in inviscid flows, U, can be approximately expressed as the square root of the product $g_z d$, where d is a characteristic dimension of the system (here $d = 3$ cm). Thus, while in the sounding rocket ($g_z = 10^{-5}g$), $U = 0.17$ cm/s, i.e. an order of magnitude below the measured flame speed of 1 cm/s, for the parabolic flights ($g_z = 2 \times 10^{-2}g$), $U = 7.7$ cm/s. This can explain the resulting stretching and increased velocity of the flame during the flights.

4.3. TEXUS-56 sounding rocket flight and experimental results

The main objective of the TEXUS-56 campaign was to observe, using the high-speed camera, the evolution of the front structure of the flame as the fuel concentration propagation threshold was approached.

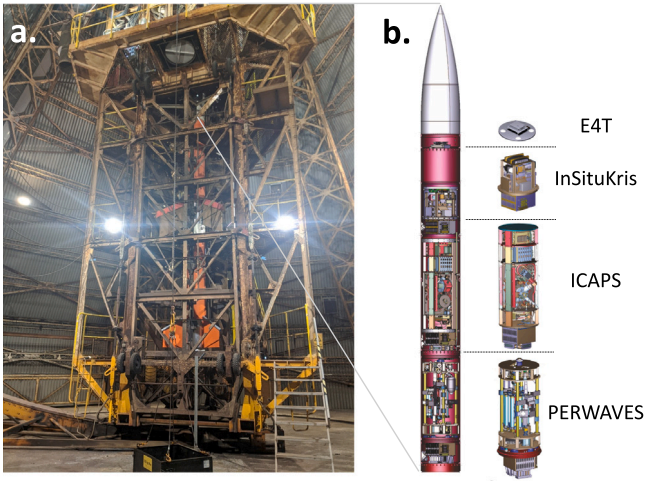

Fig. 17. TEXUS-56 sounding rocket: (a) the rocket integrated within the launch tower, (b) rocket diagram with all the experiments composing the payload.

The 40%-O_2 gas mixture was selected for these single carousel unit experiments due to its lower discreteness parameter.

The PERWAVES apparatus shared the payload of the TEXUS-56 rocket module with three other scientific experiments (Fig. 17). The ICAPS experiment studied the agglomeration behavior of micron-size particles in the environment typical of proto-planetary dust clouds. InSituKris examined the inclusion of foreign-phase particles in crystallization fronts, and a student project named AEGIS measured X-ray and gamma ray fluxes at altitudes typical for low Earth orbits.

The 5-m-long TEXUS-56 payload, weighting 386 kg, was boosted by the VSB-30 2-stage solid propellant rocket (Instituto de Aeronáutica e Espaço, Brazil) and took off from Esrange Space center in Sweden on November 15th, 2019 at 10:35 CET (Figs. 18 and 19). The flight lasted for 15 min and reached an apogee of 266 km (Fig. 18). It provided

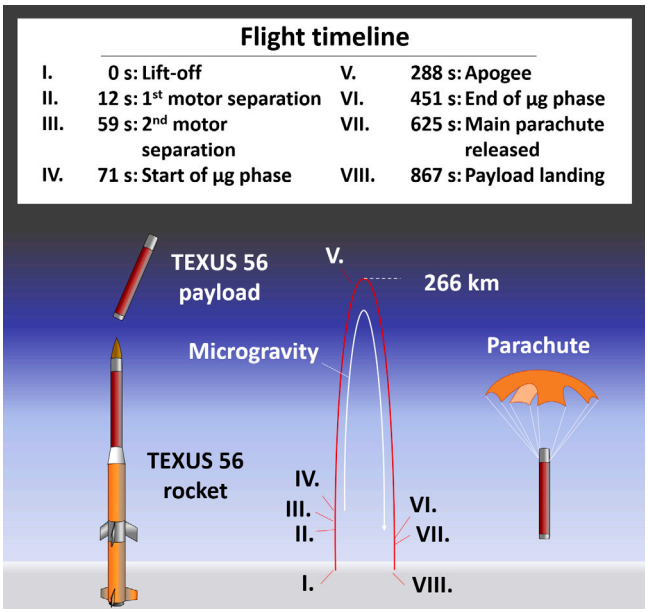

Fig. 18. Timeline of the TEXUS-56 flight stages.

Fig. 19. TEXUS-56 flight: (a) Launch of the TEXUS-56 rocket from the launch tower (courtesy of DLR-Moraba), (b) transportation of the payload back to the launch site by helicopter (credit: Samuel Goroshin).

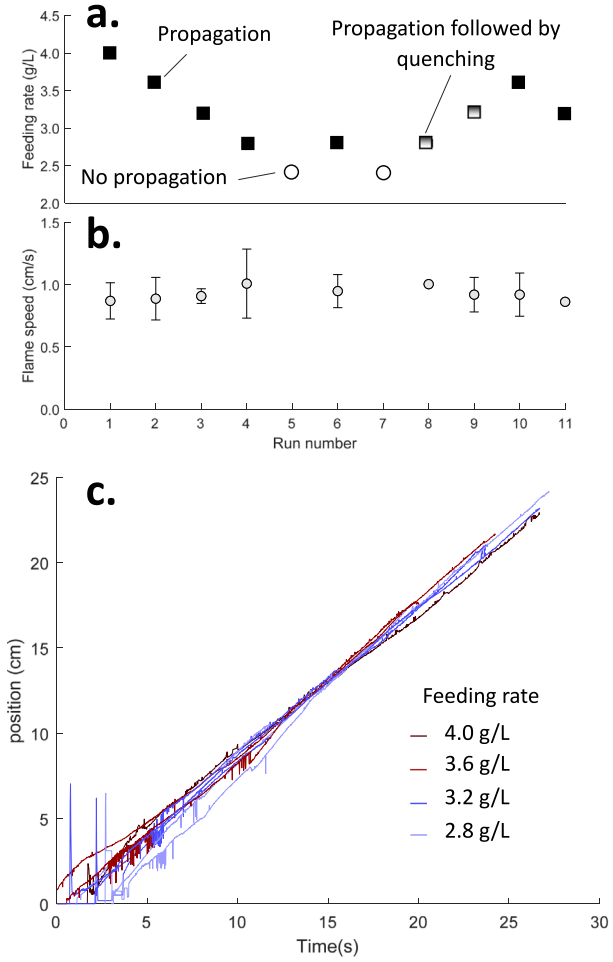

Fig. 20. TEXUS-56 results: (a) Iron powder feeding rates, (b) measured flame speed, (c) sample flame propagation traces.

6 min of freefall conditions for the on-board experiments. After re-entry and deployment of the parachute, the payload landed safely and was recovered by a helicopter (Fig. 19).

A total of 11 combustion runs were performed in all 9 tubes under free-fall conditions during the TEXUS-56 mission (Fig. 20(a)). Contrary to the MAXUS-9 flight, the operators did not need to intervene, and the experiment followed the pre-programmed experimental algorithm. The flight objectives of achieving the flame propagation threshold have been met. The flame quenched when fuel concentration was reduced close to the flame propagation limit and then demonstrated partial propagation and quenching following the algorithm-guided oscillations of the fuel concentration near the quenching concentration limit.

The modification of the ignition system led to a considerable improvement in the flame speed measurements. Traces of the flame position over time (Fig. 20(b)) confirmed that flame propagation on TEXUS-56 was free of the distortions observed on MAXUS-9 caused by the propane-ignition system. Similar to MAXUS-9 experiments, the measured flame propagation speed was around 0.8–1.0 cm/s and showed no noticeable dependence on the fuel feeding rate (compare Fig. 20(b) with Fig. 11(b)). It is also important to note that the flame propagation speeds in the rocket microgravity environment were three to five times slower than flames under the same conditions using the same apparatus in the low-gravity parabolic flight experiments (c.f. Fig. 16). This difference provides experimental confirmation of a strong flame sensitivity to the residual g levels and g-jitters in parabolic flights and justification for the need of a true low-g environment for the study of percolating flames.

In order to assess the actual concentration of iron particles in suspension, the images from the particle-counting system were analyzed postflight. These images showed a decreasing quality after the first experimental run, and a significant decrease in the signal level was observed that was much stronger than would be expected by the linear decrease in feeding rate (see runs 1–5 in Fig. 20(a)). Through ground-based testing and investigation of the images, the current working hypothesis is that some of the iron powder escaped from the tube, and its presence may have led to a partial line-of-sight obstruction of the imaging system shown in Fig. 14. It is the objective of current investigations to identify whether the presence of powder was caused by a malfunction of the dispersion or of the exhaust system.

High-quality close-up images of the flame front were recorded by both the high-speed camera (Miro C210) at the rate of 1000 fps and the flame structure camera (Basler ace acA1300-60gm) operated at 60 fps. As predicted by theory, the roughness of the 2-dimensional

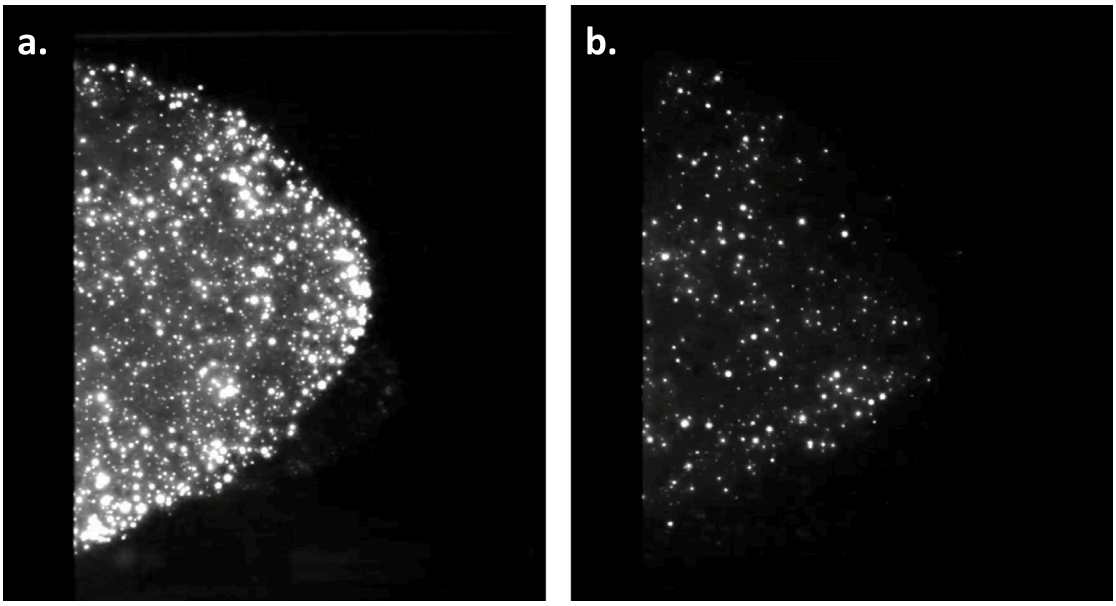

Fig. 21. Images of flame front recorded by high-speed camera: (a) at higher concentration and (b) at lower concentration (shown on frames from parabolic flights).

projection of the front increases with decrease of the fuel concentration and becomes especially prominent for flames near the propagation limit (Fig. 21(b)). With concentration approaching the flame propagation limit, the combustion events become sparser in space and time to the point when only a few burning particles are visible in each frame. The ignition positions of particles become random and they do not produce the appearance of a continuous flame front. This flame behavior closely mimics predictions by theoretical calculations [10,12,14]. These show that, at low values of the discreteness parameter and near-limit fuel concentrations, the flame propagates through local thermal connections formed between constellations of randomly positioned particles, thereby demonstrating the stochastic/statistical behavior typical of a percolating system.

5. Conclusions

An apparatus for microgravity research of flames in solid fuel suspensions on board autonomous space vehicles was designed, built, and successfully operated during two sounding rocket flights. The apparatus permits the observation of laminar flames propagating in transparent quartz tubes through uniform, quiescent suspensions of solid fuel particles in the size range of tens of microns. A suite of optical diagnostics monitors the particle cloud uniformity and the particle volumetric concentration, and permits a close-up high-speed filming of the flame structure, filming of the flame propagation process along the total length of the tube, and the acquisition of flame emission spectra. An algorithm operated by several photodiodes, which indicate the flame arrival at designated positions in the tube, controls the automatic experiment operation and permits intervention by ground-based operators.

Experiments on flame propagation in iron particle suspensions in oxygen/xenon gas mixtures were performed in two consecutive sounding-rocket flights: MAXUS-9 in 2017 and TEXUS-56 in 2019. The observed independence of the flame speed on the particle burning rates has confirmed that combustion occurs in the theoretically predicted discrete flame propagation regime, which is a prerequisite for the occurrence of percolating-flame behavior. The change in the flame appearance observed with a decrease in the fuel concentration is also in accord with theoretical modeling of the percolating flame structure.

Due to the statistical nature of percolating flames, their experimental study requires a large number of trials. Such experiments are only possible on long-duration orbital and sub-orbital platforms. The importance of the problem of percolating reaction-diffusion waves, which encompasses many fields of modern science, and the considerable difficulties encountered in their theoretical research motivates future sounding-rocket and space-based experiments.

Acknowledgments

The PERWAVES series of experiments were funded under the European Exploration Envelope Programme (E3P) of ESA. A. Verga, S. Vincent-Bonnieu, and W. Sillekens gratefully acknowledge ESA for granting the permission to publish this work. Funding was also provided by the Canadian Space Agency through the Flights and Fieldwork for the Advancement of Science and Technology (FAST) Grant Program. Student work was supported by the Panda Faculty Scholarship of the Trottier Institute for Sustainability in Engineering and Design (TISED), Canada and the Doctoral Research Scholarships Program for International Students (DS) of the Fonds de recherche du Québec - Nature et technologie (FRQNT), Canada.

The authors would also like to thank the Swedish Space Corporation (SSC) and DLR-Moraba for both successful MAXUS-9 and TEXUS-56 rocket flight campaigns in Esrange, as well as the team at the National Research Council of Canada (NRC) in Ottawa, particularly D. Gowanlock, for the flawless parabolic flight campaign. A special mention goes to P. Cordes (Airbus) for his valuable help as integrator and operator of the PERWAVES module.

Declaration of competing interest

The authors declare that they have no known competing financial interests or personal relationships that could have appeared to influence the work reported in this paper.

References

[1] T. Halpin-Healy, Y.-C. Zhang, Kinetic roughening phenomena, stochastic growth, directed polymers and all that. Aspects of multidisciplinary statistical mechanics, Phys. Rep. 254 (4) (1995) 215–414, http://dx.doi.org/10.1016/0370-1573(94)00087-J.

[2] A.M. Turing, The chemical basis of morphogenesis, Philos. Trans. R. Soc. Lond. Ser. B Biol. Sci. 237 (641) (1952) 37–72, http://dx.doi.org/10.1098/rstb.1952.0012.

[3] M. Kardar, G. Parisi, Y.-C. Zhang, Dynamic scaling of growing interfaces, Phys. Rev. Lett. 56 (1986) 889–892, http://dx.doi.org/10.1103/PhysRevLett.56.889.

[4] N. Provatas, T. Ala-Nissila, M. Grant, K. Elder, L. Piché, Scaling, propagation, and kinetic roughening of flame fronts in random media, J. Stat. Phys. 81 (3–4) (1995) 737–759, http://dx.doi.org/10.1007/BF02179255.

[5] N. Provatas, T. Ala-Nissila, M. Grant, K.R. Elder, L. Piché, Flame propagation in random media, Phys. Rev. E 51 (1995) 4232–4236, http://dx.doi.org/10.1103/PhysRevE.51.4232.

[6] M. Myllys, J. Maunuksela, M. Alava, T. Ala-Nissila, J. Merikoski, J. Timonen, Kinetic roughening in slow combustion of paper, Phys. Rev. E 64 (2001) 036101, http://dx.doi.org/10.1103/PhysRevE.64.036101.

[7] A. Rogachev, A. Mukas'yan, Experimental verification of discrete models for combustion of microheterogeneous compositions forming condensed combustion products (Review), Combust. Explos. Shock Waves 51 (1) (2015) 53–62, http://dx.doi.org/10.1134/S0010508215010050.

[8] S. Goroshin, J. Lee, Y. Shoshin, Effect of the discrete nature of heat sources on flame propagation in particulate suspensions, Symp. Combust. 27 (1) (1998) 743–749, http://dx.doi.org/10.1016/S0082-0784(98)80468-2.

[9] J. Beck, V. Volpert, Nonlinear dynamics in a simple model of solid flame microstructure, Physica D 182 (1) (2003) 86–102, http://dx.doi.org/10.1016/S0167-2789(03)00119-2.

[10] F.-D. Tang, A.J. Higgins, S. Goroshin, Effect of discreteness on heterogeneous flames: Propagation limits in regular and random particle arrays, Combust. Theory Model. 13 (2) (2009) 319–341, http://dx.doi.org/10.1080/13647830802632184.

[11] S. Goroshin, F.-D. Tang, A.J. Higgins, Reaction-diffusion fronts in media with spatially discrete sources, Phys. Rev. E 84 (2) (2011) 027301, http://dx.doi.org/10.1103/PhysRevE.84.027301.

[12] F.-D. Tang, A.J. Higgins, S. Goroshin, Propagation limits and velocity of reaction-diffusion fronts in a system of discrete random sources, Phys. Rev. E 85 (3) (2012) 036311, http://dx.doi.org/10.1103/PhysRevE.85.036311.

[13] J. Keizer, G.D. Smith, S. Ponce-Dawson, J.E. Pearson, Saltatory propagation of Ca2+ waves by Ca2+ sparks, Biophys. J. 75 (2) (1998) 595–600, http://dx.doi.org/10.1016/S0006-3495(98)77550-2.

[14] F.Y. Lam, X. Mi, A.J. Higgins, Front roughening of flames in discrete media, Phys. Rev. E 96 (1) (2017) 013107, http://dx.doi.org/10.1103/PhysRevE.96.013107.

[15] F.Y. Lam, X. Mi, A.J. Higgins, Dimensional scaling of flame propagation in discrete particulate clouds, Combust. Theory Model. 24 (3) (2020) 486–509, http://dx.doi.org/10.1080/13647830.2019.1703044.

[16] P. Julien, J. Vickery, S. Goroshin, D.L. Frost, J.M. Bergthorson, Freely-propagating flames in aluminum dust clouds, Combust. Flame 162 (11) (2015) 4241–4253, http://dx.doi.org/10.1016/j.combustflame.2015.07.046.

[17] A. Wright, A.J. Higgins, S. Goroshin, The discrete regime of flame propagation in metal particulate clouds, Combust. Sci. Technol. 188 (11–12) (2016) 2178–2199, http://dx.doi.org/10.1080/00102202.2016.1211877.

[18] M. McRae, P. Julien, S. Salvo, S. Goroshin, D.L. Frost, J.M. Bergthorson, Stabilized, flat iron flames on a hot counterflow burner, Proc. Combust. Inst. 37 (3) (2019) 3185–3191, http://dx.doi.org/10.1016/j.proci.2018.06.134.

[19] W.E. Mason, K.V. Saunders, Recirculating flow in vertical columns of gas-solid suspension, J. Phys. D: Appl. Phys. 8 (14) (1975) 1674–1685, http://dx.doi.org/10.1088/0022-3727/8/14/011.

[20] P.D. Ronney, Understanding combustion processes through microgravity research, Symp. Combust. 27 (2) (1998) 2485–2506, http://dx.doi.org/10.1016/S0082-0784(98)80101-X.

[21] D.R. Ballal, A.G. Gaydon, Flame propagation through dust clouds of carbon, coal, aluminium and magnesium in an environment of zero gravity, Proc. R. Soc. Lond. Ser. A Math. Phys. Eng. Sci. 385 (1788) (1983) 21–51, http://dx.doi.org/10.1098/rspa.1983.0003.

[22] D.L. Urban, P. Ferkul, S. Olson, G.A. Ruff, J. Easton, J.S. T'ien, Y.-T.T. Liao, C. Li, C. Fernandez-Pello, J.L. Torero, G. Legros, C. Eigenbrod, N. Smirnov, O. Fujita, S. Rouvreau, B. Toth, G. Jomaas, Flame spread: Effects of microgravity and scale, Combust. Flame 199 (2019) 168–182, http://dx.doi.org/10.1016/j.combustflame.2018.10.012.

[23] M. Mikami, Y. Yoshida, T. Seo, T. Sakashita, M. Kikuchi, T. Suzuki, M. Nokura, Space-based microgravity experiments on flame spread over randomly distributed n-decane-droplet clouds: Overall flame-spread characteristics, Microgravity Sci. Technol. 30 (4) (2018) 535–542, http://dx.doi.org/10.1007/s12217-018-9637-2.

[24] S. Gallier, J.F. Guery, Regression fronts in random sphere packs: Application to composite solid propellant burning rate, Proc. Combust. Inst. 32 (2) (2009) 2115–2122, http://dx.doi.org/10.1016/j.proci.2008.06.017.

[25] O. Rabinovich, P. Grinchuk, B. Khina, A. Belyaev, Percolation combustion: Is it possible in SHS?, Int. J. Self-Propag. High Temp. Synth. 11 (3) (2002).

[26] P.S. Grinchuk, Combustion of heterogeneous systems with a stochastic spatial structure near the propagation limits, J. Eng. Phys. Thermophys. (2013) 875–887, http://dx.doi.org/10.1007/s10891-013-0907-y.

[27] M. Schiulaz, C.R. Laumann, A.V. Balatsky, B.Z. Spivak, Theory of deflagration in disordered media, Phys. Rev. E 95 (2017) 032103, http://dx.doi.org/10.1103/PhysRevE.95.032103.

[28] M. Schiulaz, C.R. Laumann, A.V. Balatsky, B.Z. Spivak, Theory of combustion in disordered media, Phys. Rev. E 97 (2018) 062133, http://dx.doi.org/10.1103/PhysRevE.97.062133.

[29] S. Goroshin, F.-D. Tang, A.J. Higgins, J.H. Lee, Laminar dust flames in a reduced-gravity environment, Acta Astronaut. 68 (7–8) (2011) 656–666, http://dx.doi.org/10.1016/j.actaastro.2010.08.038.

[30] A. Schütte, TEXUS and MAXUS preparations for the future, in: Eur. Sp. Agency, Special Publ. ESA SP-700, 2011.

[31] F. Maggi, S. Dossi, C. Paravan, L.T. DeLuca, M. Liljedahl, Activated aluminum powders for space propulsion, Powder Technol. 270 (2015) 46–52, http://dx.doi.org/10.1016/j.powtec.2014.09.048.

[32] E.W. Price, Recent advances in solid propellant combustion instability, Symp. Combust. 12 (1) (1969) 101–113, http://dx.doi.org/10.1016/S0082-0784(69)80395-4.

[33] E.L. Dreizin, Metal-based reactive nanomaterials, Prog. Energy Combust. Sci. 35 (2) (2009) 141–167, http://dx.doi.org/10.1016/j.pecs.2008.09.001.

[34] R.K. Eckhoff, Explosion hazards in the Process Industries, Explos. Hazards Process Ind., Elsevier, 2006, http://dx.doi.org/10.1016/C2013-0-15503-1.

[35] W. Peukert, C. Wadenpohl, Industrial separation of fine particles with difficult dust properties, Powder Technol. 118 (1–2) (2001) 136–148, http://dx.doi.org/10.1016/S0032-5910(01)00304-7.

[36] D.B. Beach, A.J. Rondinone, B.G. Sumpter, S.D. Labinov, R.K. Richards, Solid-state combustion of metallic nanoparticles: New possibilities for an alternative Energy Carrier, J. Energy Resour. Technol. 129 (1) (2006) 29–32, http://dx.doi.org/10.1115/1.2424961.

[37] J.M. Bergthorson, S. Goroshin, M. Soo, P. Julien, J. Palecka, D. Frost, D. Jarvis, Direct combustion of recyclable metal fuels for zero-carbon heat and power, Appl. Energy 160 (2015) 368–382, http://dx.doi.org/10.1016/j.apenergy.2015.09.037.

[38] J.M. Bergthorson, Recyclable metal fuels for clean and compact zero-carbon power, Prog. Energy Combust. Sci. 68 (2018) 169–196, http://dx.doi.org/10.1016/j.pecs.2018.05.001.

[39] E.Y. Shafirovich, A.A. Shiryaev, U.I. Goldshleger, Magnesium and carbon dioxide: A rocket propellant for Mars missions, J. Propuls. Power 9 (2) (1993) 197–203, http://dx.doi.org/10.2514/3.23609.

[40] S. Goroshin, A.J. Higgins, J.S. Lee, Powdered magnesium-carbon dioxide propulsion concepts for mars missions, in: 35th Joint Propulsion Conference and Exhibit, 1999, p. 2408, http://dx.doi.org/10.2514/6.1999-2408.

[41] S. Goroshin, A.J. Higgins, M. Kamel, Powdered metals as fuel for hypersonic ramjets, in: 37th Joint Propulsion Conference and Exhibit, American Institute of Aeronautics and Astronautics, Reston, Virigina, 2001, http://dx.doi.org/10.2514/6.2001-3919.

[42] J. Palečka, J. Sniatowsky, S. Goroshin, A.J. Higgins, J.M. Bergthorson, A new kind of flame: Observation of the discrete flame propagation regime in iron particle suspensions in microgravity, Combust. Flame 209 (2019) 180–186, http://dx.doi.org/10.1016/j.combustflame.2019.07.023.

[43] S. Battaglioli, A.J. Robinson, S. McFadden, Influence of natural and forced gravity conditions during directional columnar solidification, Int. J. Heat Mass Transfer 126 (2018) 66–80, http://dx.doi.org/10.1016/j.ijheatmasstransfer.2018.05.151.

[44] Ansys® Academic Research Fluent, Release 19.1.

[45] R. Verjus, J.-R. Angilella, Critical Stokes number for the capture of inertial particles by recirculation cells in two-dimensional quasisteady flows, Phys. Rev. E 93 (5) (2016) 053116, http://dx.doi.org/10.1103/PhysRevE.93.053116.

[46] J.-R. Angilella, Probability of noise-induced separatrix crossing for inertial particles in flows, Phys. Rev. Fluids 4 (5) (2019) 054304, http://dx.doi.org/10.1103/PhysRevFluids.4.054304.

[47] Y.B. Zeldovich, G.I. Barenblatt, V.B. Librovich, G.M. Makhviladze, The Mathematical Theory of Combustion and Explosions, Consultants Bureau, New York, 1985.

[48] C.W. Bale, E. Bélisle, P. Chartrand, S.A. Decterov, G. Eriksson, A.E. Gheribi, K. Hack, I.H. Jung, Y.B. Kang, J. Melançon, A.D. Pelton, S. Petersen, C. Robelin, J. Sangster, P. Spencer, M.A. Van Ende, FactSage thermochemical software and databases, 2010-2016, CALPHAD, Comput. Coupling Phase Diagr. Thermochem. 54 (2016) 35–53, http://dx.doi.org/10.1016/j.calphad.2016.05.002.

[49] H.G. Wolfhard, W.G. Parker, Temperature measurements of flames containing incandescent particles, Proc. Phys. Soc. Sect. B 62 (8) (1949) 523–529, http://dx.doi.org/10.1088/0370-1301/62/8/306.

[50] R.A. Yetter, G.A. Risha, S.F. Son, Metal particle combustion and nanotechnology, Proc. Combust. Inst. 32 (2) (2009) 1819–1838, http://dx.doi.org/10.1016/j.proci.2008.08.013.

[51] S. Fischer, M. Grubelich, A survey of combustible metals, thermites, and intermetallics for pyrotechnic applications, in: 32nd Joint Propulsion Conference and Exhibit, American Institute of Aeronautics and Astronautics, Reston, Virigina, 1996, pp. 1–13, http://dx.doi.org/10.2514/6.1996-3018.